TERAHERTZ DIFFUSE REFLECTORS AND THEIR EFFECTS ON GROUP DELAY DISPERSION AND COMMUNICATION PERFORMANCE

By

RUSS MESSENGER

Bachelor of Science in Electrical Engineering

Oklahoma State University

Stillwater, OK

2019

Submitted to the Faculty of the
Graduate College of the
Oklahoma State University
in partial fulfillment of
the requirements for
the Degree of
MASTER OF SCIENCE
December 2021

TERAHERTZ DIFFUSE REFLECTORS AND

THEIR EFFECTS ON GROUP DELAY DISPERSION

AND COMMUNICATION PERFORMANCE

Thesis Approved:

Dr. John O'Hara

Thesis Adviser

Dr. Sabit Ekin

Dr. Weili Zhang

Name: RUSS MESSENGER

Date of Degree: DECEMBER 2021

Title of Study: TERAHERTZ DIFFUSE REFLECTORS AND THEIR EFFECTS ON GROUP DELAY DISPERSION AND COMMUNICATION PERFORMANCE

Major Field: ELECTRICAL ENGINEERING

Abstract: Engineered terahertz diffuse reflectors were created using mixtures of paint and varying amounts of aluminum powder to improve the reflectivity and scattering properties of surfaces. The performance of these reflectors is measured and analyzed using broadband terahertz spectroscopy. The effects of temporal dispersion caused by rough surface reflections on wireless terahertz communication is quantified and predicted using communication simulations. A scattering model using stochastic methods is used to describe rough surfaces, including the effects group delay dispersion caused by rough surface reflections. This model was validated using broadband terahertz spectroscopy to compare measured and simulated results. The modeled channel transfer function was used in a quadrature phase shift keyed (QPSK) communication simulation to find the expected symbol error rate with respect to surface roughness. Based on these simulations, a distinct dispersion limit in which group delay dispersion from rough surface reflections begins to cause symbol errors is found.

TABLE OF CONTENTS

LIST OF TABLES

Table Page

LIST OF FIGURES

Figure Page

CHAPTER I

INTRODUCTION

The ability to use terahertz (THz) radiation for communication purposes is becoming closer and closer to a reality every day. The need for more bandwidth and higher data rates is pushing researchers to look at higher frequencies [1], [2]. Many applications pushing the need for higher data rates, including streaming video [3], video games , telemedicine [4], education [5] and the Internet of Things (IoT) [6]. Fifth generation (5G) wireless communications have recently come out and will ease some of the burden on the current infrastructure, but the need for higher data traffic will continue to increase. Sixth generation (6G) networks will need to be developed to prevent future data bottlenecks [7] and, the use of terahertz frequencies will likely be needed.

The terahertz band is between 0.1-10 THz or 3-0.03 mm. This puts the band between the microwave bands and the infrared light bands in the electromagnetic spectrum. Frequency bands above 275 GHz have yet to be fully allocated by the FCC [8], making it very appealing for new communication methods and technologies. The terahertz band exhibits qualities similar to both the infrared and microwave bands. Due to the smaller wavelengths compared to microwave; many challenges exist in creating technologies to use it effectively for communications compared to lower frequencies. One major challenge is providing large signal coverage [9], [10]. The wavelength of THz radiation increases the directivity of antennas. This increase in directivity is

very beneficial for line-of-sight (LOS) communications in overcoming free space loss. This large directivity, however, will lead to very narrow beam paths and reduce total signal coverage. This has led many to claim that terahertz wireless links will be limited to LOS applications [11]; however, it should be noted that LOS may not be possible in many situations [12]. Non-line-of-sight (NLOS) communications will have to be used in these situations. Very accurate beam steering could potentially help, but in complex environments receivers may have to rely on diffused or scattered terahertz radiation to acquire a signal. Therefore, it is important to know how THz radiation interacts with surfaces, and how to overcome the challenges to using terahertz radiation.

Due to the different scattering properties of materials over the terahertz range, microwave channel models are, at many times, unsuitable for terahertz frequencies. Many of these models are currently being developed and are discussed in more detail in section 2. The model used in the communication simulations is described in chapter IV.

The multipath effects and delay spread due to dispersion from rough surfaces are mentioned in many studies [9], [13], [14], yet none of the studies go into the impact of temporal dispersion on the relationship of achievable data rate and symbol error rate (SER). In this thesis, a combination of broadband, terahertz time-domain measurements and simulation are used to investigate the impact of group delay dispersion, induced by rough surface reflections on symbol error rate at various high data rates. Specifically, this thesis will investigate textured surfaces, common in many homes and buildings, on the terahertz channel. Therefore, textured drywall samples are used as scattering surfaces. Using a channel model based on reflection measurements from these textured samples, the simulated digital wireless communication performance is measured using quadrature phase shift keying (QPSK) modulation at rates of 10-50 gigabaud (GBd) at a carrier frequency of 0.25 THz. A unique finding from this work is that a distinct "dispersion limit" on system performance is found as a function of scattering surface height

distribution. Beyond this limit, GDD can cause a massive increase of the SER, such that communication may become impractical at high data rates.

Section 1. Terahertz Reflectors

There are many methods to overcome signal coverage limitations using non-line-of-sight (NLOS) channels. This includes the use of diffuse [12], [14] and engineered [15], [16] surfaces which spatially disperse an otherwise highly directive beam to reach multiple receivers. In addition, the properties of many common building materials such as plaster, wood, cinderblock, and glass [7], [17] have been investigated for their uses as reflectors and/or scatterers. It is important to note that many of these surfaces are considered smooth reflectors at microwave frequencies but have significant surface roughness at terahertz frequencies. This is due to the surface's standard deviation in roughness or height becoming significantly large compared to the wavelength of the signal. Many metasurfaces have also been studied for specific communication channel purposes, such as mirroring spatial beam dispersion or diffusion, and multi-beam generation [16], [18], [19]. Dai developed an active metamaterial to perform QPSK modulation [20]. Qi *et al.* created a coding metasurface using a Pancharatnam-Berry phase concept to achieve a full 360 degrees phase coverage [21]. Sima *et al.* designed a meta-mirror to produce frequency selective scattering using a coding metasurface [22]. Momeni *et al.* designed a tunable diffuse coding metasurface using graphene [23]. Srivastava made a flexible terahertz meta-sensor in 2017 [24]. Many terahertz frequency selective surfaces (FSS) have been designed. Li *et al.* designed a bandpass FSS for terahertz frequencies in 2017 [25]. Guo *et al.* developed a hybrid finite difference time domain method of measuring terahertz FSSs [26]. Xiang Li *et al.* developed high power high pass and low pass FSSs for terahertz [27]. None of these studies addressed the impact of temporal dispersion induced by the device.

Section 2. Terahertz Modeling

Much terahertz channel modeling work has already been reported in recent literature. These models are already being developed, based on experimental and simulation work [10], [13], [28], [29]. Sheikh *et al*. discusses two different models, the Beckmann-Kirchhoff and Effective Roughness models, showing that both are capable of predicting total received power of diffusely scattered terahertz waves [10]. Piesiewicz *et al*. developed modified Fresnel equations and ray tracing to simulate wall and ceiling scattering of terahertz radiation, quantifying absolute power and propagation patterns in indoor scenarios [13], and Priebe *et al*. measured the channel impulse response and transfer function of an indoor propagation environment, capturing power delay profile and reflection loss for wood, plaster, and plastic surfaces [9]. Wei *et al.* present integral equation and vector radiative transfer methods suitable for modeling backscatter from metallic and dielectric rough surfaces, providing an excellent fit to measured terahertz data [28], [29]. Dikmelik *et al*. introduced an analytical model to approximate reflections in the specular direction off rough surfaces leading to an explanation of fading, specifically the roll-off of spectral magnitude with increasing scattering surface height distribution [30]. Ma *et al*. and references therein comprise a review of several scattering measurements to date. Ma *et al*. also showed empirical terahertz communication performance results for an NLOS channel, in which the signal experienced a single reflection between the receiver and transmitter, using an amplitude shift keyed system at 100, 200, 300, and 400 GHz [7]. The results proved that a 1 Gbps channel with low bit error rate is achievable even in NLOS operation, over reflection incidence angles between 20 to 60 degrees. Again, none of these studies addressed the topic of temporal dispersion induced by the channel, nor its impact in communication error rates.

Section 3: Group Delay Dispersion

To understand the approach to this thesis work, it is critical to understand the phenomenon of group delay dispersion (GDD). GDD is the second order derivative of the frequency-dependent phase θ of a signal or the first order derivative of the group delay (GD).

$$GD = \frac{\partial \theta}{\partial \omega} \quad (1)$$

$$GDD = \frac{\partial^2 \theta}{\partial \omega^2} \quad (2)$$

where ω is the angular frequency in rad/sec. GDD is used to describe the temporal dispersion of a signal. This is similar to group velocity dispersion (GVD), used in fiber optic communications, which is the GDD normalized to 1 unit (typically 1 meter) of distance. GDD, however, is much more useful for describing the second order dispersion caused by reflections from surfaces since a distance is ill-defined for the phase accumulation induced by a single surface. When GDD is present, the frequency components of a signal will have different propagation times. This temporally spreads out a signal as shown in Fig. 1.

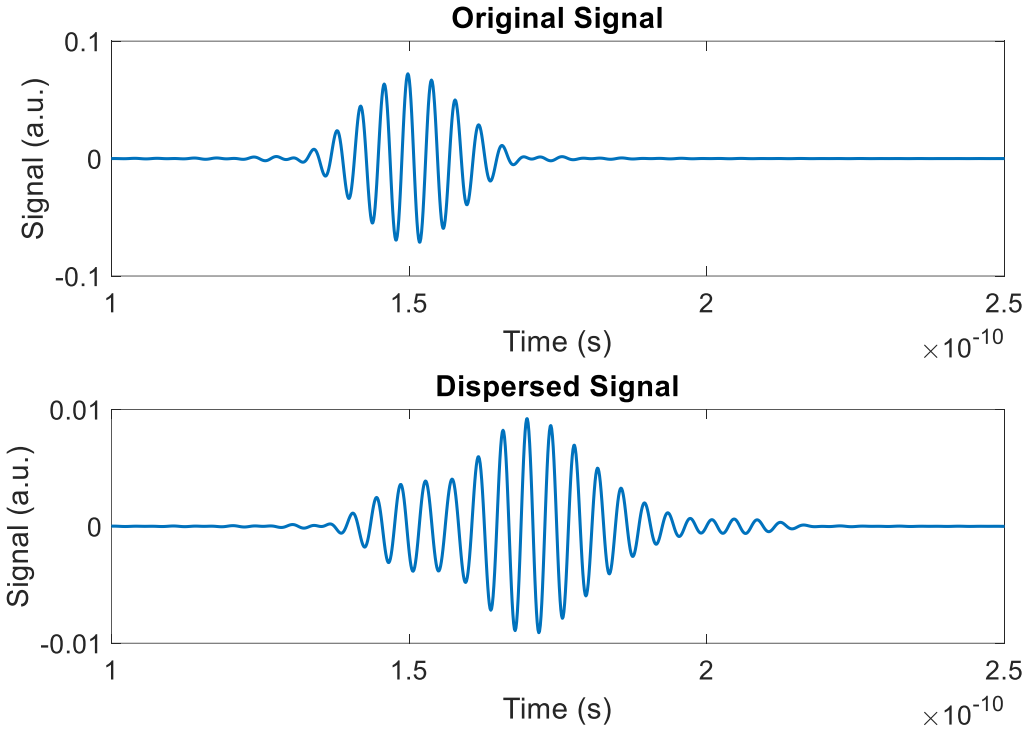

Fig. 1: Filtered time-domain terahertz pulse before and after being dispersed by a rough surface reflection.

Section 4: Organization of Thesis

The rest of the thesis follows this structure. Chapter II details the creation of the samples used to reflect and scatter terahertz signals. Chapter III discusses the methods and results of THz band measurements of the sample from chapter II. Chapter IV discusses a THz band channel model and simulation thereof. This will include the simulation verification and its implications to overall THz symbol error rate (SER) from reflections off rough surfaces. Finally, chapter V is the conclusion of this thesis with any final remarks.

CHAPTER II

SAMPLE CREATION AND CHARACTERIZATION

Section 1. Sample Preparation

Samples were made with the goal to enhance terahertz band connectivity by coating drywall with special metal "doped" paints. The paints are doped by adding metal powders to the paint mixture before applying it to a surface. The original hypothesis was that adding metal powders to paint would increase the reflectivity of the surface, and that using a coarse powder would create a textured surface that would spatially diffuse reflected terahertz radiation.

All the drywall samples used in the experiments were cut from a single 0.5-inch -thick panel of Georgia-Pacific ToughRock Drywall. The control sample consisted of an untextured 100 mm × 100 mm section of drywall, painted with an indoor, 100% acrylic paint manufactured by the Sherwin-Williams Company (Fig. 2a). The other samples were cut to near the same size as the control (±2 mm) and then coated with the same paint doped with various concentrations of aluminum (Al) powder. The metal "doped" paint samples were made using two different Al powders. The first was a fine, 3.0-4.5 micron spherical aluminum powder from Alfa Aesar. The spherical Al powder mixed well with the paint. The fine powder paint was able to be applied to the drywall in the same manner as the un-doped paint. However, at the maximum concentration tested, the paint mixture was much thicker and harder to apply to the drywall smoothly. There

was also a slight discoloration of the paint. The second was a coarse, 149-297 micron Al powder from Atlantic Equipment Engineers. The coarse powder was selected to provide a texture to the drywall (enhancing spatial dispersion) and to improve the reflectivity of the surface, which would increase the received signal strength for NLOS communications. The coarse powder paint was more difficult to mix compared to the fine powder paint. However, there was no discoloration to the paint using the coarse Al powder. The paint was mixed with each Al powder at the following mass (powder) to volume (paint)ratios: 500 mg/mL, 250 mg/mL, 100mg/mL, 50 mg/mL, 25 mg/mL, 10 mg/mL, and 5 mg/mL. The doped paints were applied with a paint brush to the drywall samples in the same manner as the undoped paint. Due to the larger particle size of the coarse Al powder, a highly visible texture was created (Fig 1b).

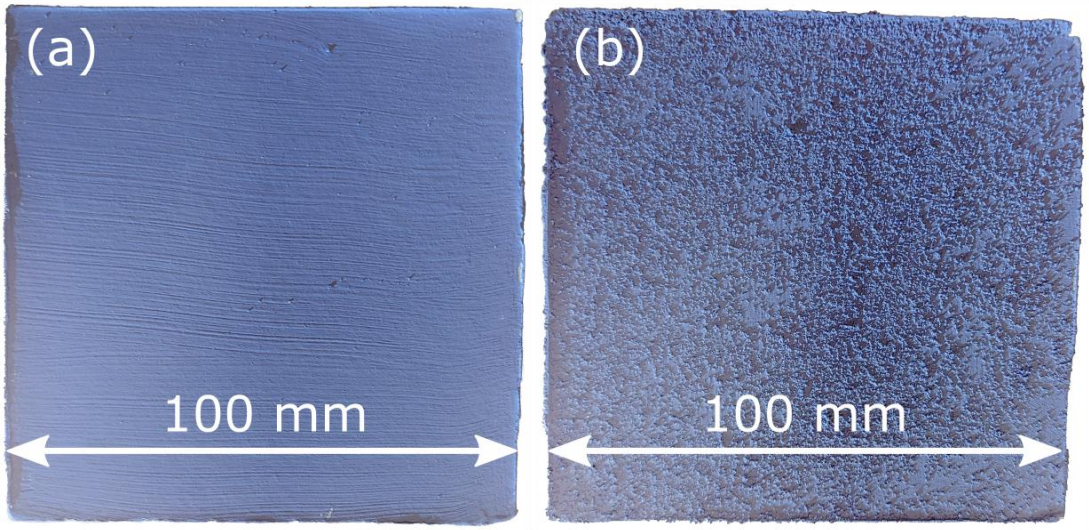

Fig. 2: Drywall samples with (a) un-doped, and (b) 500mg/mL coarse Al powder doped paint. [31]© 2021 IEEE

Section 2. Sample Texture Measurements

The surface roughness of the samples was measured using a contact profilometer in which a digital plunge micrometer with 5 μm accuracy was affixed in the *y*-axis (vertical axis) to an *xz*-combination translation stage upon which the sample was mounted. A custom tip was made

for the micrometer using a 198 micron radius ruby ball and was used as the profilometer stylus. The profilometer is shown in Fig. 3.

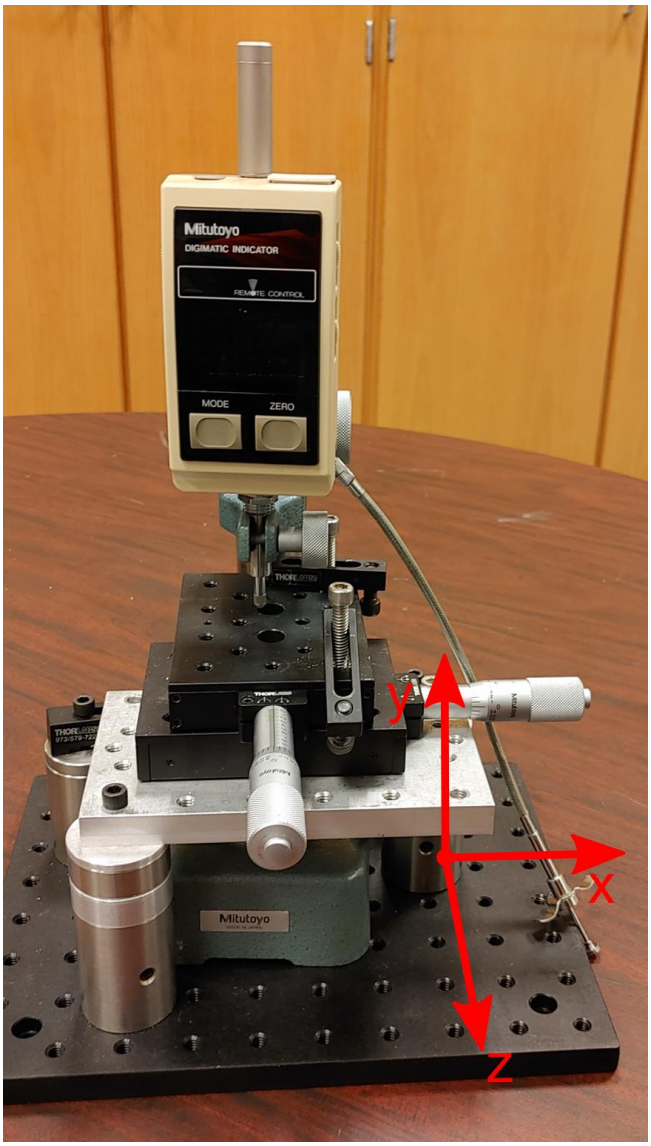

Fig. 3: Surface profilometer used to obtain surface height profile of drywall samples.

These measurements were taken to determine the physical properties of our samples. The surface height profile data were manually collected from the sample with 500 mg/mL doping over an area of 19.05 mm × 2.67 mm, using a transverse step size of $\Delta x = \Delta z = 127$ μm in both x and z dimensions. This produced a data set of $K = 22$ one-dimensional surface profiles, each profile

being comprised of $R = 151$ data points for a total sample set of 3,322 profile measurements from the sample. Similarly, 1,661 points ($K = 11$ one-dimensional profiles of length $R = 151$) were collected from the undoped sample, using the same Δx and Δz. Fig. 4 shows a surface plot and the surface height histogram generated from the 500 mg/mL coarse sample data, taken from the drywall sample shown in Fig. 2b. A subset of surface height measurements was also collected with $\Delta x = 63.5$ μm to ensure sufficient resolution in the measurements. These affected very few measurements and none more than 4% in surface height.

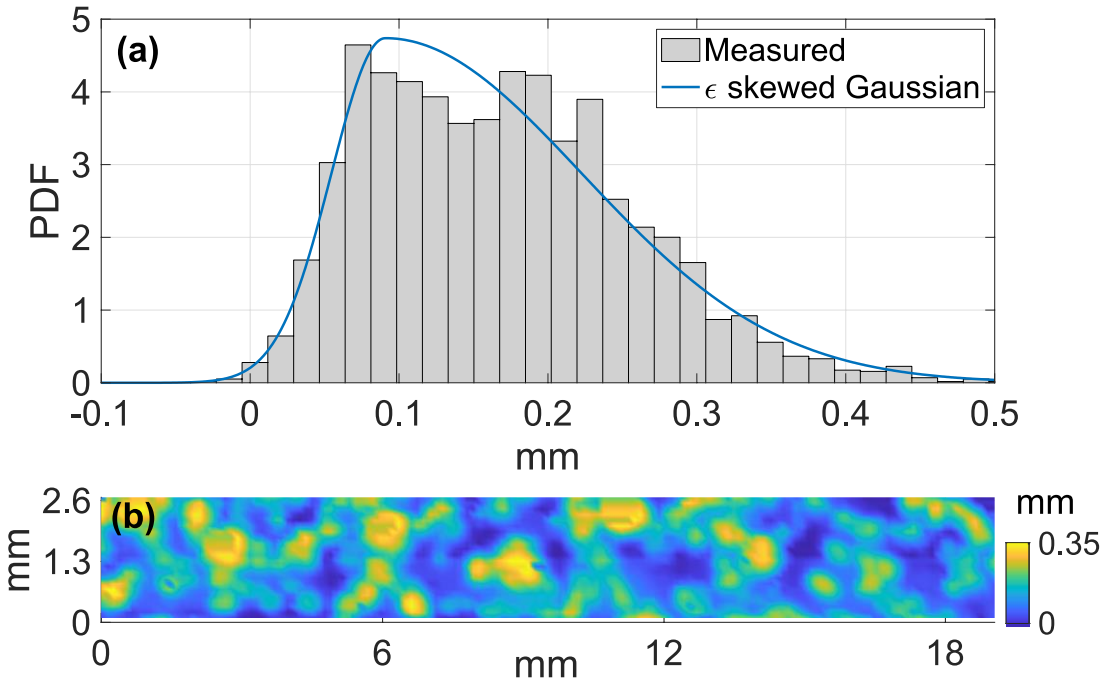

Fig. 4: (a) Normalized histogram of measured surface height variations with corresponding epsilon skewed gaussian PDF. (b) Measured surface height profile, where height is indicated by the color map. [31]© 2021 IEEE

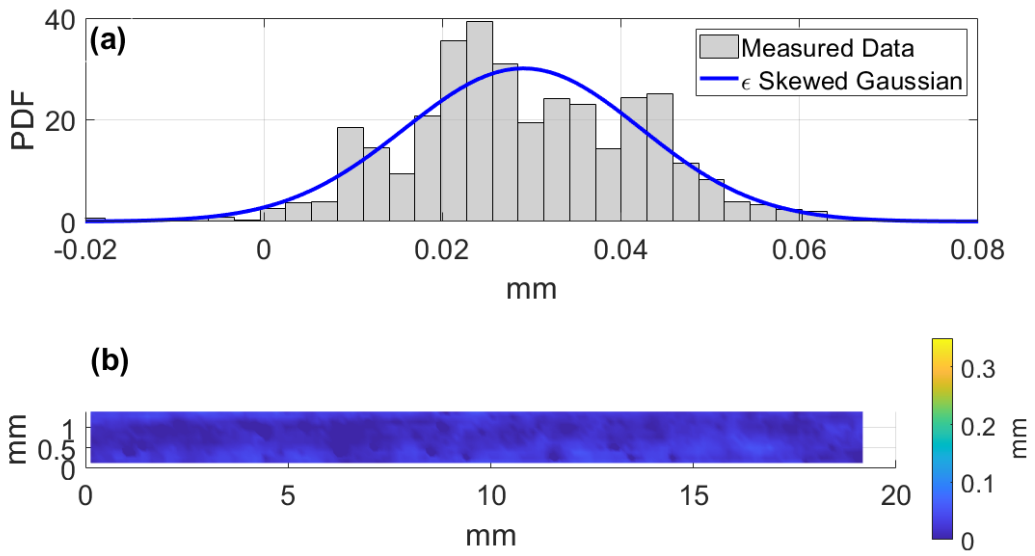

Fig. 5: (a) Normalized histogram of un-doped painted sample. (b) Measured surface height profile.

Fig. 5 shows the histogram and surface height plot of the un-doped painted drywall sample. It is clear that the coarse powder increased the surface roughness significantly compared to the un-doped painted sample.

The surface height for the 500 mg/mL coarse powder doped sample was found to fit an epsilon skewed Gaussian distribution having the probability density function (PDF) [32] of

$$f_o(y) = \begin{cases} \frac{1}{\gamma\sqrt{2\pi}} \exp\left(-\frac{(y-\eta)^2}{2\gamma^2(1+\varepsilon)^2}\right) & \text{if } y < 0 \\ \frac{1}{\gamma\sqrt{2\pi}} \exp\left(-\frac{(y-\eta)^2}{2\gamma^2(1-\varepsilon)^2}\right) & \text{if } y \geq 0 \end{cases}, \tag{3}$$

where $\varepsilon = -0.5794$, $\eta = 0.0895$ mm, and $\gamma = 0.0841$ mm are the skewness parameter, mode (or location parameter), and scale parameter, respectively [32]. Table 1 includes other meaningful characteristics of the surface height distribution for both the coarse doped and undoped paint samples. It should be clarified that the skewness parameter and the skewness of the distribution are not the same [32]. The observed positive skewness indicates that there is a relatively larger number of valleys in our sample, as compared to an unskewed Gaussian distributed surface. The

kurtosis gives a measure of the steepness the valleys and peaks of the surface profile [33]. Higher kurtosis loosely means the surface peaks and valleys are spiky or abrupt while lower kurtosis surfaces appear to transition between peaks and valleys more smoothly. In addition, from a probability distribution standpoint, a kurtosis greater than 3 implies the tails of the distribution approach zero more slowly than a normal distribution. For reference, a normal (unskewed Gaussian) distribution has a skewness of 0 and a kurtosis of 3. The non-doped sample closely matched an unskewed Gaussian distributed surface. It should be noted that many different distribution types could potentially be used to try to match the surface profile. The epsilon skewed gaussian distribution was the closest match for the 500 mg/mL coarse powder sample.

When discussing the nature of rough surface scattering, the correlation length C_L of the surface is another important physical property. It quantifies the distance by which two points on the surface must be separated before their heights are considered independent of one another. Loosely speaking, the surface can be considered "rougher" over a smaller spatial scale as the correlation length of the surface decreases. If the correlation length is very large, then the surface height changes slowly over distance. Correlation length is defined as the point where the average autocovariance of the surface $C_{avg}(\tau) = e^{-1}$.

$$C_{avg}(C_L) = e^{-1} \qquad (4)$$

In the case of discrete measured data shown above, the separation distance τ takes values $\tau = m * \Delta x$ for $m = 1,2,3, \dots, M$, where the maximum correlation distance index $M < R$. The average autocovariance $C_{avg}(\tau)$ is found by averaging the autocovariances $C_k(\tau)$ of the individual surface profiles, where the autocovariance of surface profile k is

$$C_k(\tau) = \frac{1}{\sigma_k^2 (R - M)} \sum_{r=1}^{R-M} [(H_r - \mu_k) * (H_{r+m} - \mu_k)\,]; \quad (5)$$

where σ_k is the standard deviation (or RMS height) of the surface roughness and μ_k is the mean surface height, of profile k [29]. H_k^r and H_k^{r+m} are the measured surface heights of profile k at points r and $r+m$ respectively. For our $K = 22$ by $R = 151$ data taken from the 500 mg/mL sample, the correlation length was found to be approximately $C_L = 384$ μm. For the non-doped sample, the correlation length was found to be approximately 254 μm.

TABLE 1

Sample	Mean	Variance	Skewness	Kurtosis	RMS Height
Coarse powder	167 μm	8.10 μm^2	0.7709	3.4606	89 μm
Paint only	29.0 μm	0.176 μm^2	–0.0094	3.0001	13 μm

CHAPTER III

TERAHERTZ MEASUREMENTS

Section 1: THz System Information

The terahertz measurements were performed using a terahertz time-domain spectroscopy (THz-TDS) system [34], as shown in Fig. 6. For this TDS system, the receiver was fiber-coupled to the gating laser, so it was capable of rotating around the z-axis without altering laser alignment or timing. This enabled measurement of the spatial dispersion of the scattered energy, though most of the measurements utilized a specular arrangement ($\phi = \phi_r = 45°$) to maximize received signal power. Only horizontal linear polarization (p-polarization) was used for the measurements.

Specular reflection measurements were collected from both the doped and non-doped drywall samples, as well as a first surface flat mirror, which was used as a phase and amplitude reference. The mirror was considered lossless in this analysis. Control measurements were performed using non-doped and unpainted drywall to isolate the effect of the paint alone, shown in Fig. 7. The reference mirror was measured between each sample to account for any drift of the THz-TDS system during measurements. All samples and the reference mirror were mounted such that their front surface coincided with a single-phase reference plane established by kinematic stops, as illustrated in Fig. 6. This is an imperfect scheme since the surface roughness of the samples compromised the performance of the kinematic stops. However, the stops proved

adequate, since an absolute phase reference to the reference mirror is unnecessary to demonstrate the reported phenomena. The THz-TDS system had a usable bandwidth of approximately 2.5 THz. When measuring samples, the loss reduced the usable bandwidth to around 2 THz.

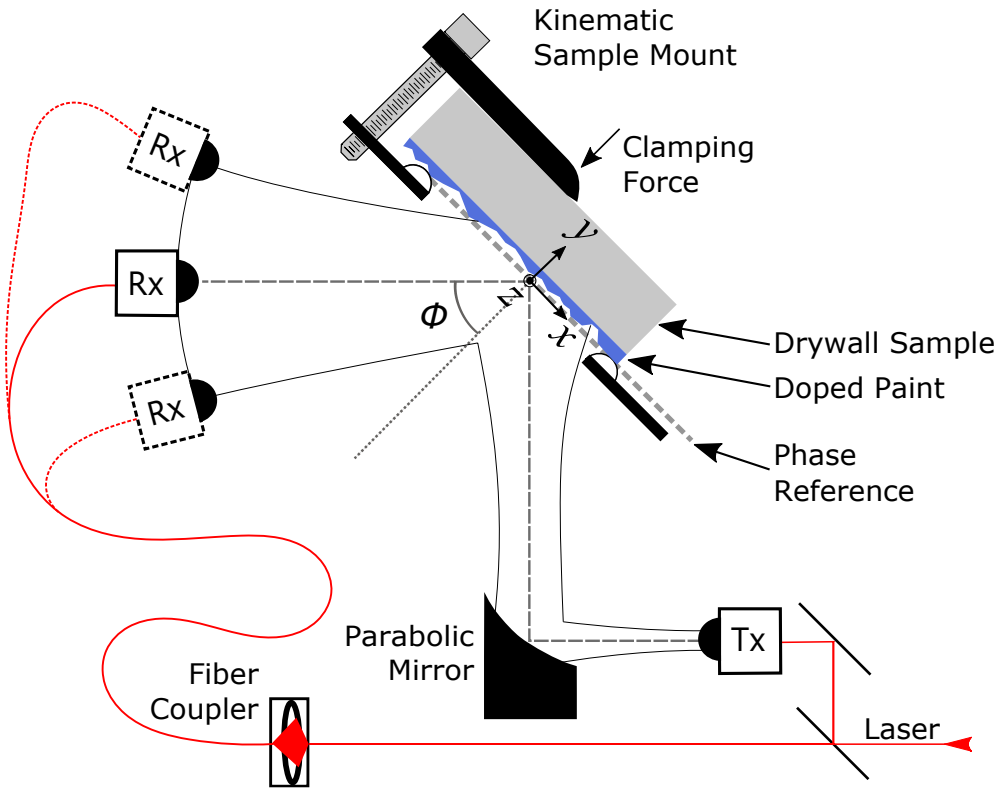

Fig. 6: THz-TDS system. Samples are mounted with the scattering face pressed lightly against kinematic stops to provide a constant phase reference. The terahertz receiver is fiber-coupled and capable of rotating around the sample mount (*z*-axis) to measure scattering in the horizontal (*xy*) plane. [31]© 2021 IEEE

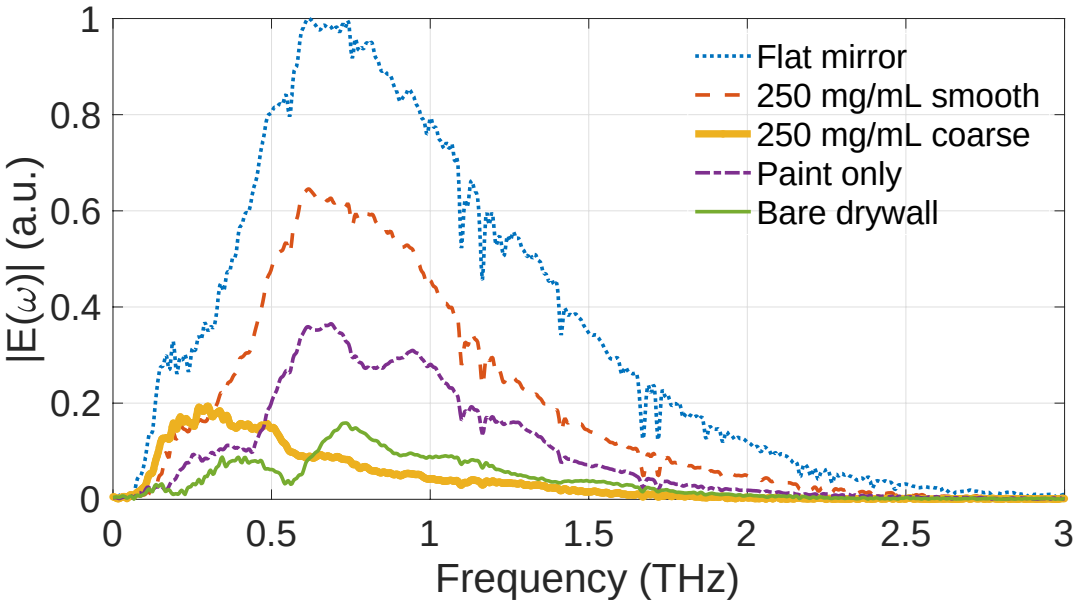

Fig. 7: Normalized frequency spectra of various measured terahertz signals. Small downward spikes, most evident on the flat mirror spectrum, were caused by residual water vapor, which was not eliminated by the dry-air enclosure around the THz-TDS system. [31]© 2021 IEEE

Section 2: Reflectivity Measurements

The reflectivity measurements were taken in the specular direction off the sample ($\phi = \phi_r = 45°$). The fine 2-4.5 micron Al powder increased the reflectivity dramatically at the 250mg/mL concentration compared to the painted control sample. This increased the reflectivity over approximately all frequencies the THz-TDS system could measure in its configuration. The coarse powder showed an increase in reflectivity for low frequencies compared to the control; however, at higher frequencies the signal strength was lower in the specular direction. This in initially suggests that the higher frequency signals are more affected by surface roughness, thus more energy is scattered. This is consistent with scattering theory, due to the surface roughness becoming significantly larger compared to the wavelength of the signal. Fig. 8 shows the change in reflectivity compared to the concentration of Al powder of both. Based on the results from Fig. 8, it is clear that there are diminishing returns for increased Al powder concentration beyond 250

mg/mL. Fig. 9 shows the received time domain waveforms of the references and the 250 mg/mL doped samples.

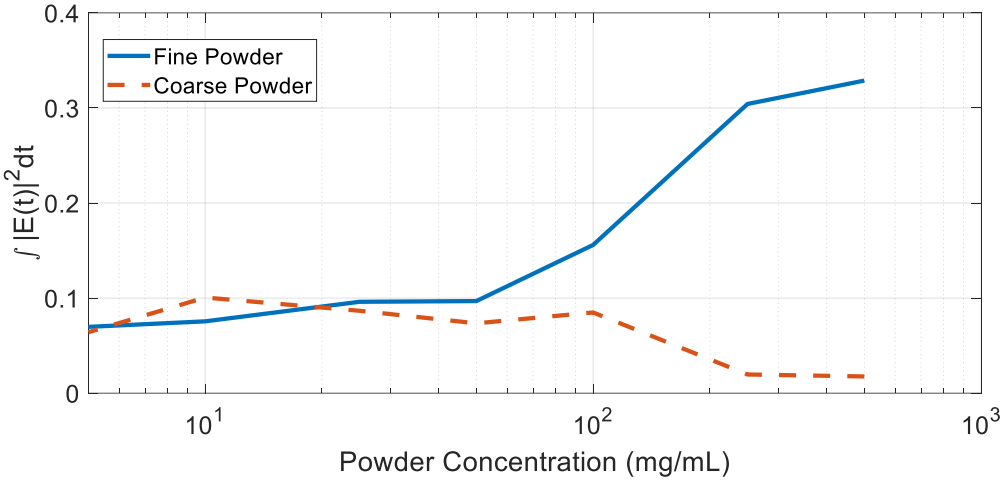

Figure 8: Comparison of fine and coarse aluminum powder samples total energy reflected compared to the reference mirror.

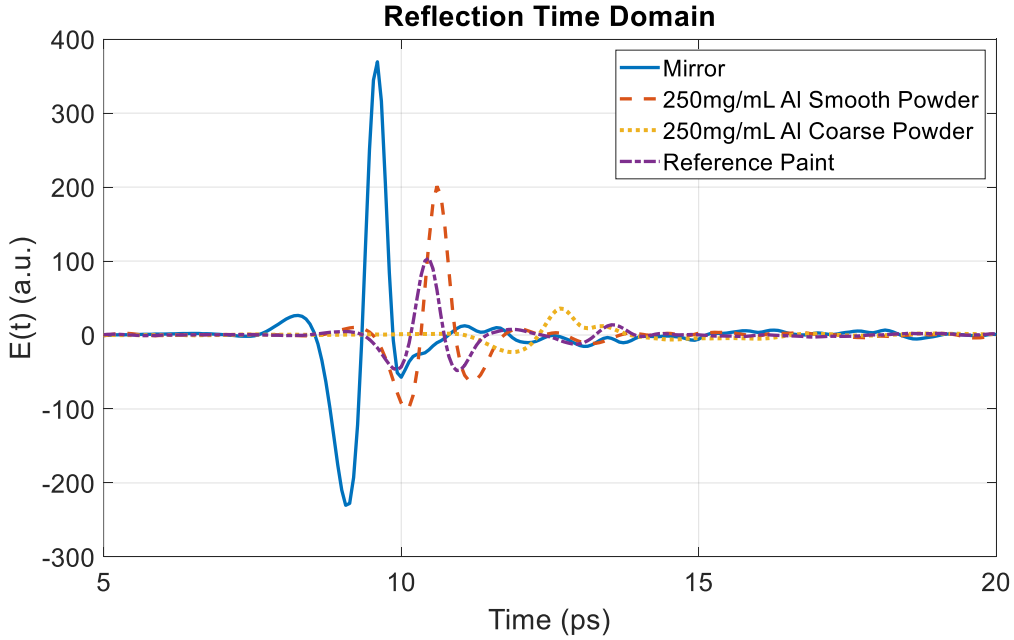

Fig. 9: Time domain measured THz pulses

Section 3: Scattering Measurements

Additional measurements were performed with the receiver positioned at varying angles ϕ to measure spatial scattering. The incidence angle on the sample was kept at 45° with the receiver arm being rotated in 1° increments over ±20° around the specular reflection angle, ϕ_r = 45°. The received signals were then squared and integrated over time to give values proportional to total received energy. The energy received around ϕ_r was much greater from the reference than it was from the coarse powder sample; however, at angles ϕ > 53° and ϕ < 32°, more energy was received from the coarse powder sample than the reference as shown by Fig 10. This unambiguously shows that power is being spatially scattered by the rough surface, but since the noise was becoming comparable to the signal strength at wider scattering angles, it was difficult to separate how much specular energy was lost to scattering versus absorption. This shows that one of the main goals of the Al powder doped paint was accomplished: the improved spatial distribution of the signal.

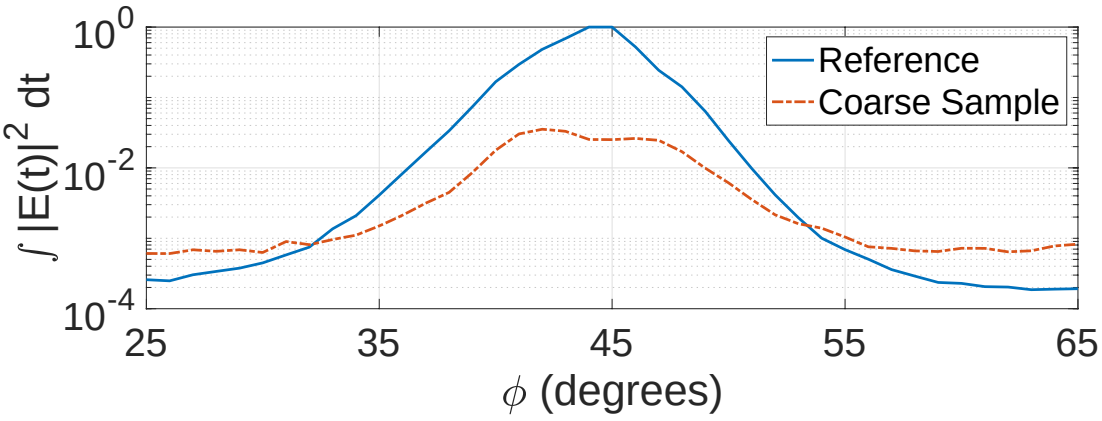

Fig. 10: Total power received at various receiver angles, where ϕ is referenced from the sample surface normal (–*y* axis), as in Fig. 6. [31]© 2021 IEEE

Another way to view the data from figure 10 is to look at individual frequency bands. To do this, the same measured time-domain data was Fourier transformed, squared, and then

integrated over a frequency band instead of time. This would determine the effective scattering within that band. The results of this calculation are shown in fig. 11 for 100 GHz channels. It should be noted that the reference beamwidth becomes smaller at higher frequencies, as expected. It also becomes very apparent that the coarse Al powder sample is scattering a large amount of energy, eventually to the point that more power is received from the coarse sample than the reference mirror at larger angles away from the specular direction.

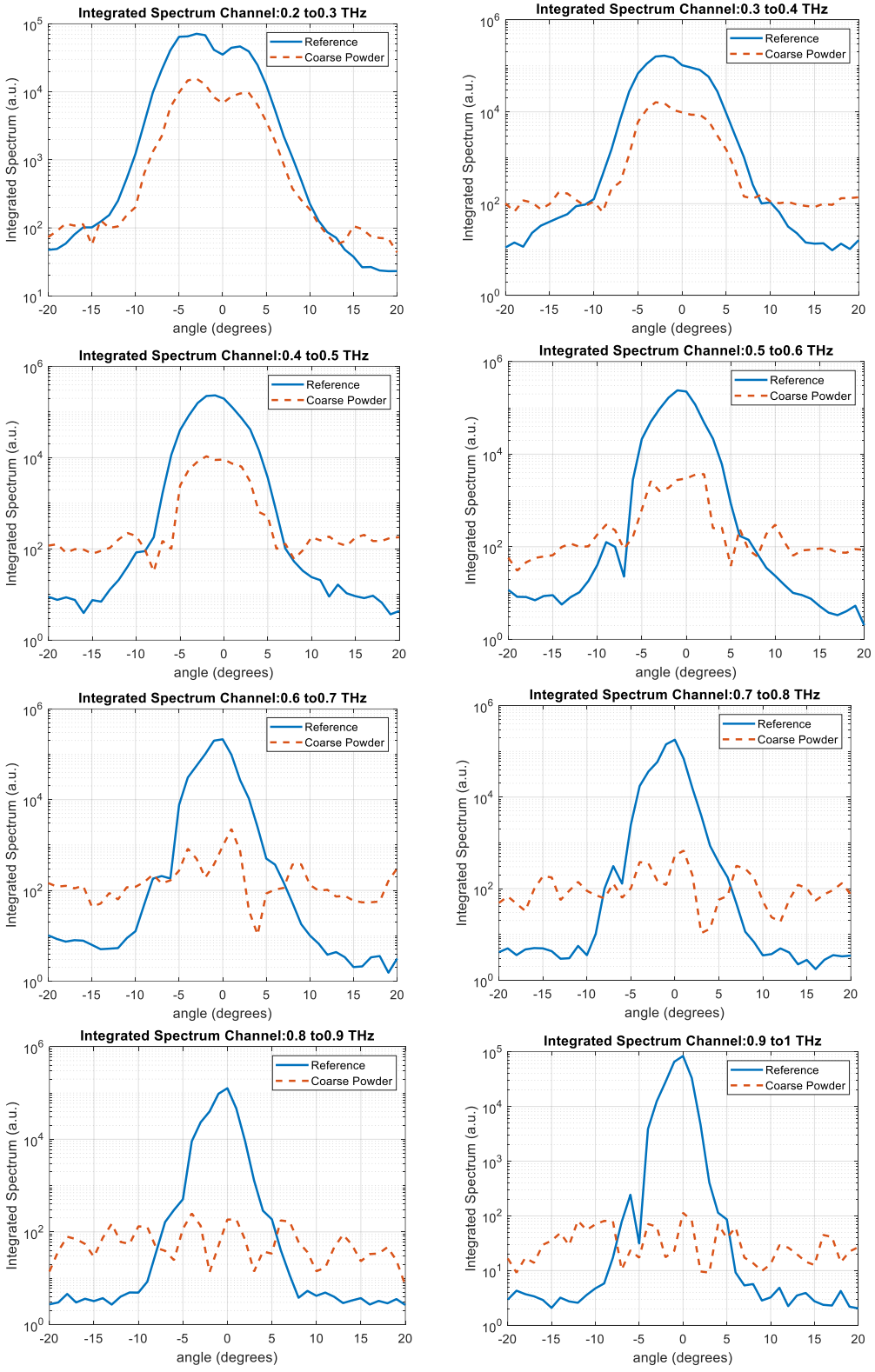

Fig. 11: Total received power at various angles for 100 GHz channels starting at 0.1 THz to 1 THz.

The effect of varying *incidence* angles ϕ_i = [35°:55°] was also investigated for specular measurements. Small changes in amplitude occurred but these would not significantly affect the GDD results reported in chapter IV. Additional measurements at more extreme angles would have to be performed to obtain more significant results; however, the sample mount would have to be modified to prevent interference with the signal.

The specular angle measurements of the 500 mg/mL sample provided interesting results when analyzing the return spectrum, especially in terms of GDD. Due to this, this sample was looked at with much more detail than the other samples to characterize how rough surfaces affect THz signals. For the additional measurements on this sample, the entire drywall sample was divided into four regions, designated C1 through C4. Fig. 12 shows a white circle to indicate the measured terahertz beam position and size on the measured regions. Each region was characterized three times using THz-TDS to ensure repeatability. Since all four regions were measured from the same overall drywall sample, these provided a good demonstration of the variety of measured waveforms that can result from a single texture application. An additional eight locations were also measured, producing a variety of spectral shapes with similar features that were differently positioned and/or scaled.

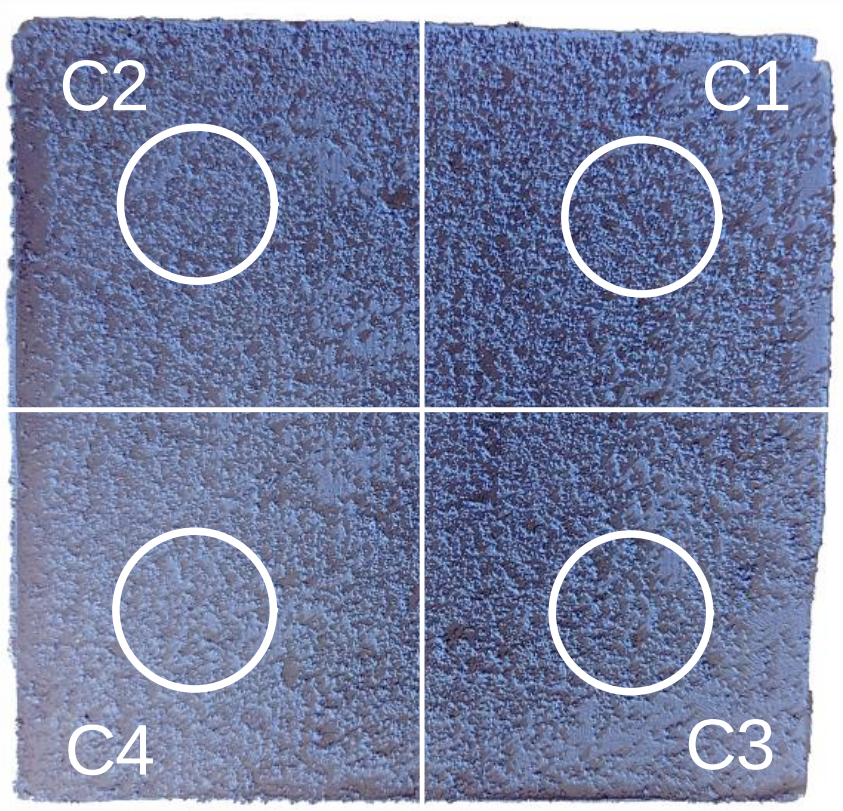

Fig. 12: Division of sample shown in Fig. 2b, showing the four regions illuminated by the terahertz beam (white circles), C1-C4. Each illumination region was approximately 20 mm in diameter. [31]© 2021 IEEE

Spectral reflection data from areas C1-C4 are shown in Fig. 13 They were obtained by taking the absolute value of the discrete Fourier transform to the measured time-domain terahertz amplitude data. Many key features of this data are explained in the next few paragraphs to better put it into the context of this thesis. Fig. 13 also includes simulated results produced by the channel model discussed in the next chapter.

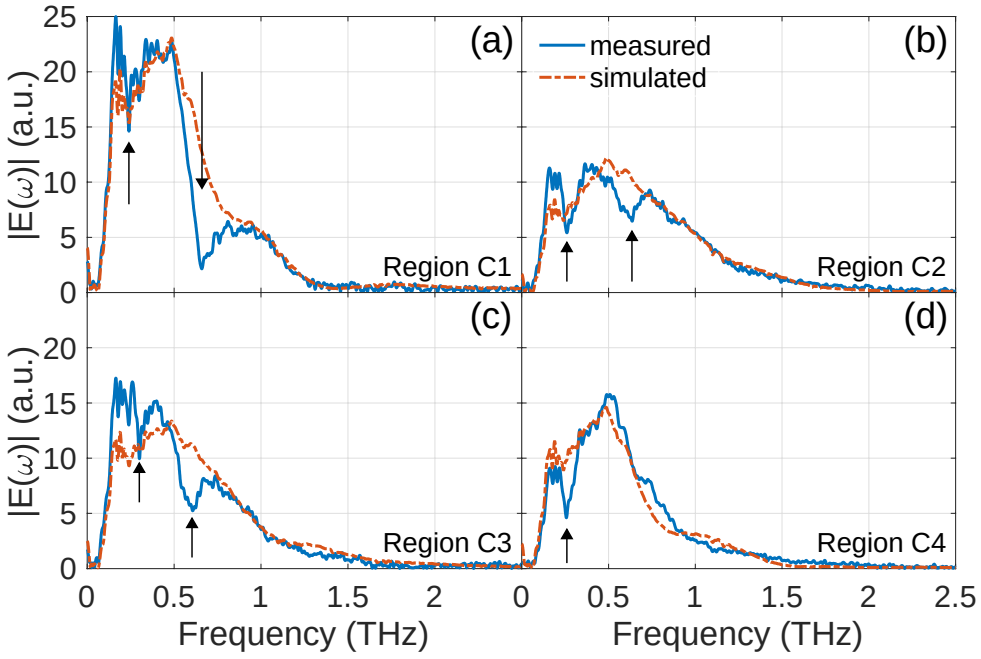

Fig. 13: Measured data from the four beam locations (C1-C4) of the 500mg/mL coarse Al powder sample, overlaid with individual (unaveraged) simulation results that exhibit similarity to the measured data, showing that the model can replicate the diversity of measured spectra. Vertical arrows designate interference nulls. [31]© 2021 IEEE

First, the bandwidth changes considerably among the measurements. Measurement C1 (Fig. 13a) had observable components only below 1.5 THz, whereas measurement C2 (Fig. 13b) had observable components to almost 2 THz. In addition, the full-width-at-half-maximum (FWHM) spectral bandwidth ranges from about 0.5 THz (C1) to 1 THz (C2). This is quite different from the results shown in Dikmelik *et al.* [30], in which a clear Gaussian frequency roll-off was observed beyond a cutoff frequency was determined by the standard deviation of surface height. This cutoff behavior assumed that the surface height varies according to a Gaussian distribution's variance [30]. Fig. 14 shows a comparison to the measured data from the sample to the expected results using calculations derived from Dikmelik's paper. The Dikmelik spectrum is calculated using the following equation, where A_0 is the reference spectrum, R is the reflectivity

of the 500 mg/mL fine Al powder sample, ω is the angular frequency, and σ_τ^2 is the variance of the time delays caused by reflecting off a rough surface.

$$A(\omega) = A_0(\omega) \exp\left(-\frac{\omega^2 \sigma_\tau^2}{2}\right) * R, \qquad (6)$$

Equation 6 is modified slightly from the equation originally shown in in [30] by the addition of the R value. This corrects for the difference in the reflectivity between the mirror and drywall sample. The fact that there was a different behavior is not surprising due to the appearance of a skewed Gaussian height distribution compared to a Gaussian height distribution reported in Dikmelik.

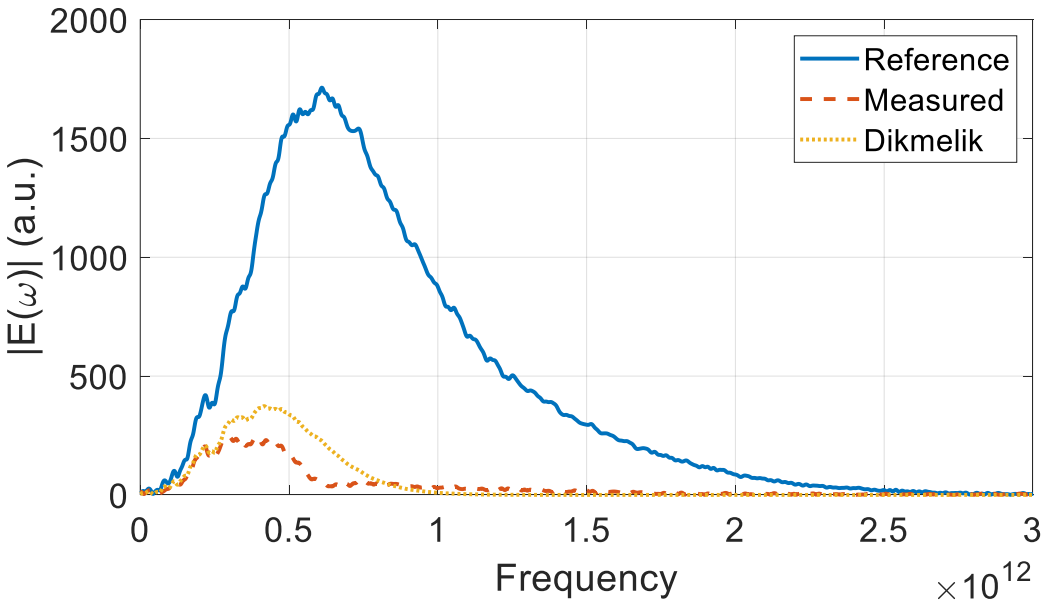

Fig. 14: Spectrum comparison using Dikmelik's model, and the data measured from C1.

The second important feature of Fig. 13 is the various locations of the interference nulls. These nulls may be the result of frequency selective fading [35] and indicate the ever-present, but random, possibility of poorer signal transmission in certain bands for static channels. Similar to spatial interference patterns observed in earlier work [12], this fading appears to be caused by

multipath effects where the roughened wall produces a delay spread within the area of the reflected beam. While some of these nulls are substantial, most are not deep enough to suggest a total loss of signal power to the extent that communications would be impossible. Nevertheless, since the frequency-domain spectra are analytic, changes in the amplitude of a signal must be accompanied by changes in the phase of a signal. Since frequency-dependent phase shifts lead to GDD (eq. 2), these spectral features can be regarded as most important in the context of the principal result of this thesis.

A third notable feature is that all the measurements have a low cutoff frequency approximately at 60 GHz. This is an inherent characteristic of the THZ-TDS system and not due to the sample. This feature appears in all the measured data including the reference mirror shown in Fig. 7.

CHAPTER IV

COMMUNICATION SYSTEM SIMULATIONS

Section 1: Reflection Model

Because the measured spectral features directly relate to the severity of GDD and the resulting communication system performance, it is necessary to develop a model capable of reproducing them. Similar to the work of Dikmelik *et al*., [30] the scattering surface was modeled as an array of planar perfect reflectors, where each element had a random height (in the $\pm y$ direction in Fig. 6) relative to the average surface position. The modeled reflector heights were randomly sampled from either the physical surface measurements (Chapter 2) or from simulated surfaces obeying the same epsilon skewed Gaussian surface profile height statistic. In this model, when a terahertz wave is reflected by the surface, the distribution of reflector heights is manifest as a superposition of irresolvable multipath reflections possessing independent, identically distributed random time delays. The assumption that the distributions of scatter heights (and corresponding time delays) are independent is valid because the region illuminated by the terahertz beam has a radius 26 times greater than the surface correlation length. In addition, the multipath reflections are temporally irresolvable because the bandwidth of the system is insufficient to resolve the numerous individual reflections that arrive within a single-digit picosecond timescale. The superposition of irresolvable multipath reflections results in temporal dispersion (delay spread).

The two-dimensional distribution of these reflectors in the *xz*-plane was ignored in our model, effectively giving each reflector of the set the same position ($x = z = 0$). While this may prevent the determination of effects due to *transverse* surface correlation lengths [12], it also isolates observed effects to the time-domain, simplifying the temporal dispersion analysis and mechanisms of causation. Again, this simplification is justified by the fact that correlation effects should be insignificant due to the large terahertz spot size relative to the surface correlation length.

To simulate the reflected wave time-domain profile, an input waveform, $a_o(t)$, is first established. For Fig. 13, an actual THz-TDS specular reflection measurement from the flat reference mirror serves as $a_o(t)$. The model then calculates a time delay t_i in the reflected wave for every reflector in the modeled surface height distribution, and these time shifts are then applied to copies of the input pulse. The resulting delayed reflected waves are finally averaged together in a superposition to make the final output waveform,

$$a(t) = \frac{S}{N} \sum_{i=1}^{N} a_o(t - t_i) \tag{7}$$

where N is the number of reflectors in the set and is established based on the beam size of the signal and the correlation length of the surface profile. A global scaling factor S accounts for losses due to diffuse scattering, material absorption, and general system inefficiencies, however it also assumes that each reflected wave of the set has the same amplitude. This is a very simplified model that can be modified in many ways to improve accuracy; however, the stochastic nature of the time delays created by the rough surface makes many of them moot.

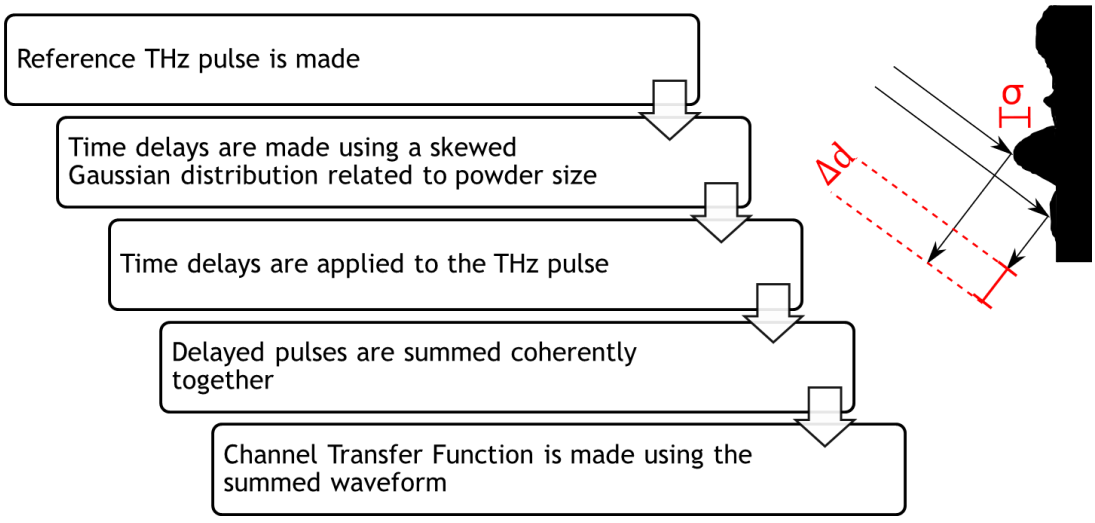

Fig 15: Diagram of the steps used to produce a channel transfer function using the model discussed in section 1.

Section 2: Model Validation

The reflected terahertz pulse spectra predicted by the model were compared against those measured in the TDS system, using an array of N = 100 reflectors with epsilon skewed, normally distributed time-delays as the model parameters. $N = 100$ was selected due to the area occupied by the total beamwidth of the system at the sample location and the surface area occupied by a particle of the coarse Al powder. One hundred thousand iterations of the simulation were performed to do a random search to find potential matches to the measured signal. New arrays of reflector heights were generated for each simulation. The use of a large number of reflector array instances (and thus time shifts t_i) allowed for the determination of the model's capability of reproducing the measured results. To illustrate, four example frequency spectra from the 100,000 simulations are shown in Fig. 16 (repeated here from Figure 13 for convenience). As in the measured data, these spectra were obtained by taking the absolute value of the Fourier transformation of the simulation's time-domain output. The model proved capable of producing

variability like measured reflection spectra and these were selected due to their similarity to actual measured data from four different areas of the textured drywall.

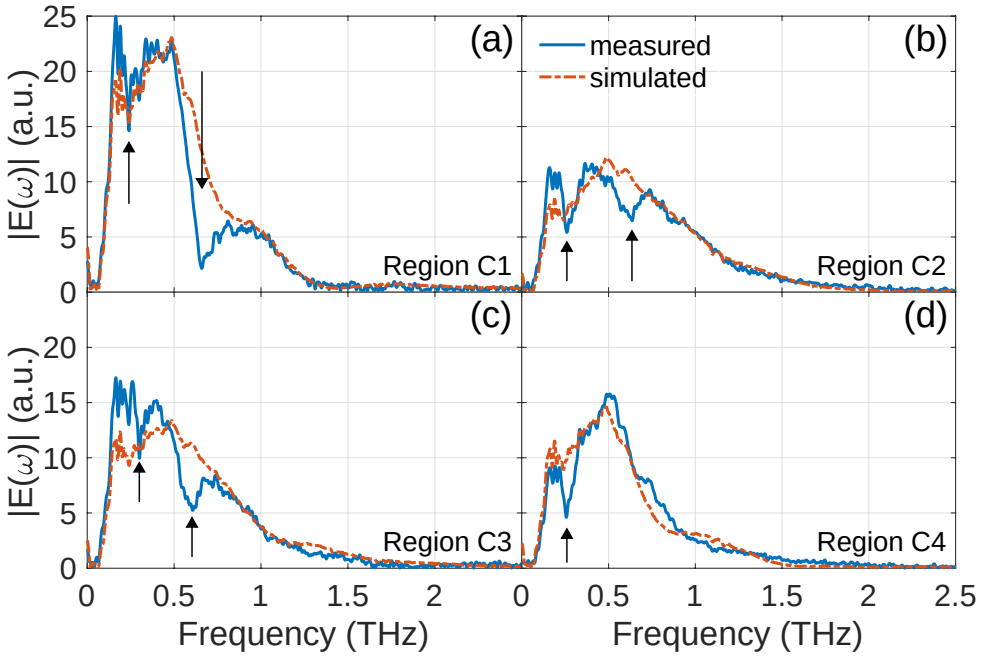

Fig. 16: Measured data from the four beam locations (C1-C4) of the 500mg/mL coarse Al powder sample, overlaid with individual (unaveraged) simulation results that exhibit similarity to the measured data, showing that the model can replicate the diversity of measured spectra. Vertical arrows designate interference nulls. [31]© 2021 IEEE

While an exact fit to the data was not expected from this approximate stochastic model, many of the measured features were reproduced by the model, including the spectral magnitudes, bandwidths, general spectrum shape, and some interference nulls. The most obvious disagreement from the selected simulations to the measured data is the location and the depth of random spectral nulls. It is not yet clear whether this is a weakness in the model, an insufficiency in the number of simulation trials, or a result of the simplistic process by which simulated data are selected for comparison; however, the model does produce random spectrum nulls within the frequency range of the measured data. In addition, the simulated null depth can reach high values consistent with measured data, although the simulated spectra shown in Fig. 16 did not. These

spectra were selected by using a least sum of differences algorithm between the measured and simulated data. The algorithm favors matching spectra based on the overall shape of the spectra, while locations and depths of frequency nulls have less weight. Apart from adjusting the scaling factor *S* to normalize out system losses, no attempt was made to fit the model spectra to the measured data. Due to the closeness of the simulated results, the scattering (channel) model can be regarded as adequate for follow-on studies of scattering, associated GDD, and its effect on communication system performance, as are described in the next section.

Section 3: Group Delay Dispersion Analysis

The effects of multipath scattering are well known in microwave and millimeter-wave wireless systems but have been studied relatively little in the terahertz regime thus far. Small-scale, frequency-dependent fading is often described as the principal penalty from multipath propagation. However, by the analyticity of the complex spectra, any frequency-dependent amplitude effect must be accompanied by some frequency-dependent change in phase (time shift and temporal dispersion). This results in large spikes in the GDD of a signal around these interference nulls. Since these nulls are approximately 100 GHz wide, and can appear almost anywhere in the usable spectrum, this means GDD is always a potential problem for high bandwidth terahertz signals. Likewise, they suggest that the presence of GDD in a particular band of interest is likely to be unpredictable, as the locations of the spectral nulls depend on the exact surface characteristics, which are stochastic and potentially variable (in the case of a moving beam). This effect on phase becomes increasingly impactful for higher bandwidth 6G signals. This model can be used to quantify these effects by simulating both GD and GDD.

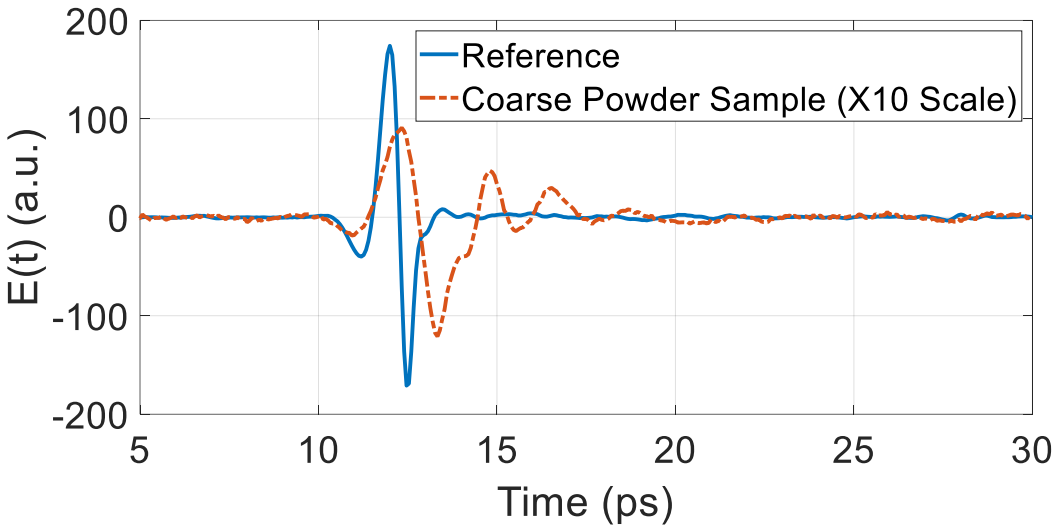

Fig. 17: Measured THz time domain signals. Note the larger amount of time for the coarse powder signal to be completed compared to the reference signal.

When the GD is variable over frequency, GDD becomes non-zero, or equivalently there is non-zero second-order dispersion in the channel that spreads out temporal waveform features [36]. Fig. 17 shows measured THz time domain waveforms of the coarse powder sample and reference mirror. In this figure, it is clear how the waveform reflected off the coarse sample has been spread out temporally. Figure 18(a) shows GDD determined from the measured reflection data of the coarse textured drywall sample and the reference mirror. This measurement was taken near the C1 area of the sample shown in Fig. 12. The bipolar spike at ~0.65 THz in the coarse sample GDD is most notable, rising well above the GDD of the reference mirror, which is expectedly near zero over most of the bandwidth. The areas below 0.15 THz and above 1.4 THz are outside the range of the THz-TDS system. This makes the GDD calculation very inaccurate due to insufficient signal-to-noise in the signal so the measured GDD below 0.15 and above 1.4 THz should be ignored. To obtain the GDD measurements between 0.15 and 1.4 THz, A very large SNR was required. To produce the plot in Fig. 18 many measurements had to be averaged together to raise the SNR to an acceptable level for the measurement to be valid.

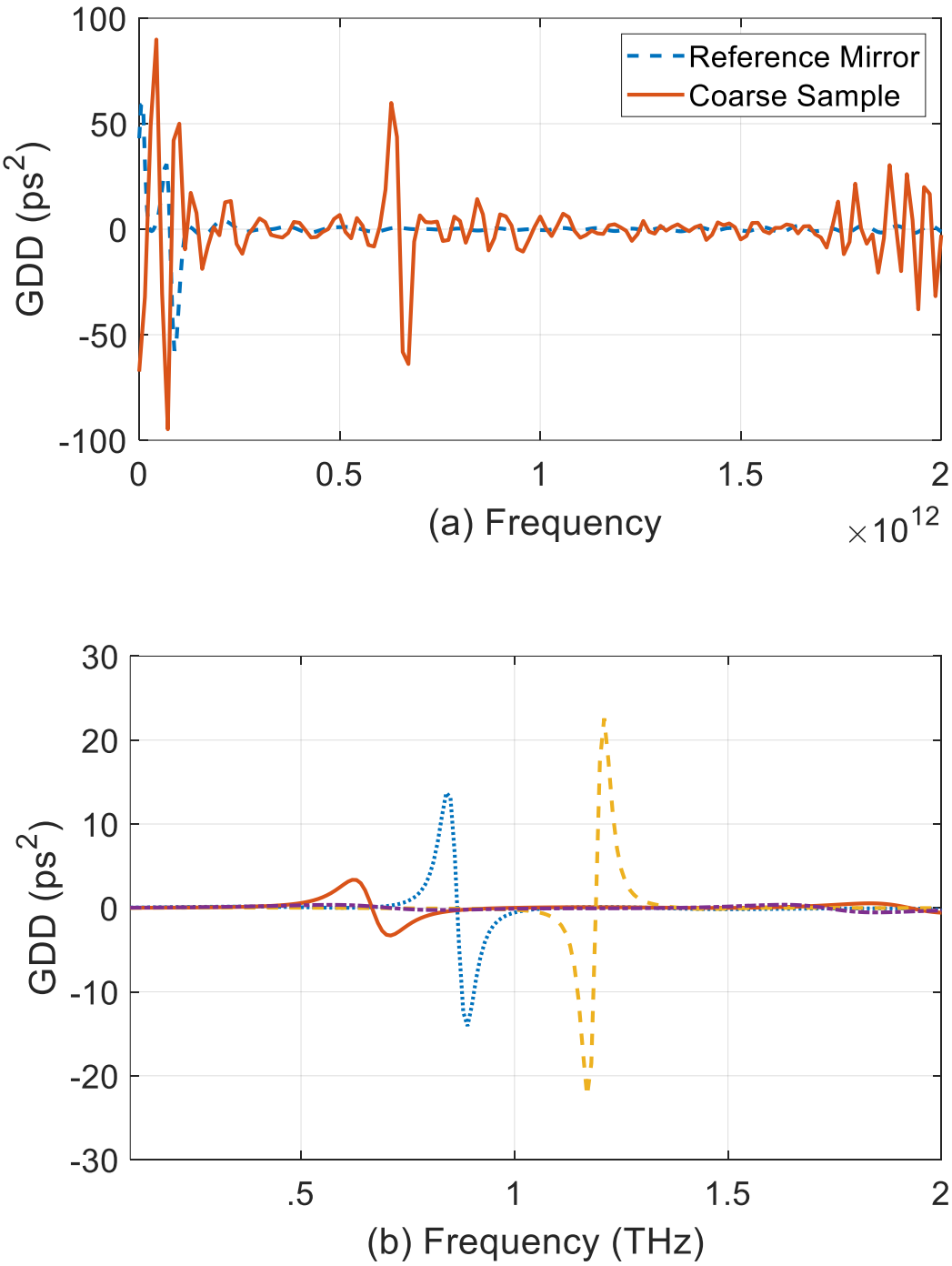

Fig. 18: (a) Measured GDD plot from textured wall sample and reference mirror. (b) Four GDD plots resulting from different random instances of the same distribution. These are simply random GDD examples produced by the model and are not correlated with the measurements in Fig. 13.

Fig. 18(b) shows four examples of the GDD predicted by our model when terahertz waves reflect off textured surfaces using random surface height values measured from the 500 mg/mL coarse powder sample. Note that because the model essentially disregards transverse particle extent, the mean value of the particle size has no dispersive effect and only produces a constant phase shift, which contributes nothing to GD or GDD. Like the measured data, the plots confirm a bipolar GDD response can reach substantial levels over bandwidths approaching 100 GHz. Again, given the random nature of texturing, this large band of dispersion can occur almost anywhere between 0.3-1.0 THz. Coarser textures (larger σ) exhibit stronger GDD bands at lower frequencies, while still having a major effect on higher frequencies. Substantial GDD effects begin to occur once σ of the surface becomes comparable to the operating wavelength, since such a surface would impart substantial phase shifts to the reflected copies of the signal.

The measured GDD data are noticeably more jagged than the simulated data. This appears to be mostly due to system noise, which is not a factor in the model. In addition, the second order derivative in Eq. 2 is very sensitive to frequency step size and signal noise, both of which can artificially create large oscillations in the resultant GDD. Frequency step size is governed by the durations of the time-domain signals, which are necessarily limited to avoid Fabry-Perot reflections from the back side of the samples. The reflection model does not take this into account. Regardless, the measured and simulated GDD appear to be similar in form, bandwidth, and general amplitude, supporting the model validity.

As stated before, GDD causes temporal dispersion of the waveform, which in turn can cause neighboring symbols in a digital data stream to blend into one another, resulting in inter-symbol interference (ISI) [37]. Therefore, as GDD increases, ISI also increases, resulting in a larger SER. In this way, GDD directly impacts what SERs are achievable for a particular data rate. Conversely, GDD will impart a reduced upper limit on data rates for a fixed low SER, even

in the absence of noise [38], which is detrimental since the primary motivation of terahertz wireless is to achieve extremely high data rates.

Section 4: Error Rate Simulation Methodology

Although plots such as Fig. 18 are useful in demonstrating the varied GDD profiles that can be produced by a textured surface, they are not as useful in predicting the precise impact of that surface on the fidelity or data-carrying capacity of an incident communication signal. To determine whether the GDD presented in Fig. 18 is truly "substantial," it is necessary to quantify the expected SER – that is, the probability that a reflection from the surface will cause sufficient distortion to the waveform such that a communication symbol is received in error.

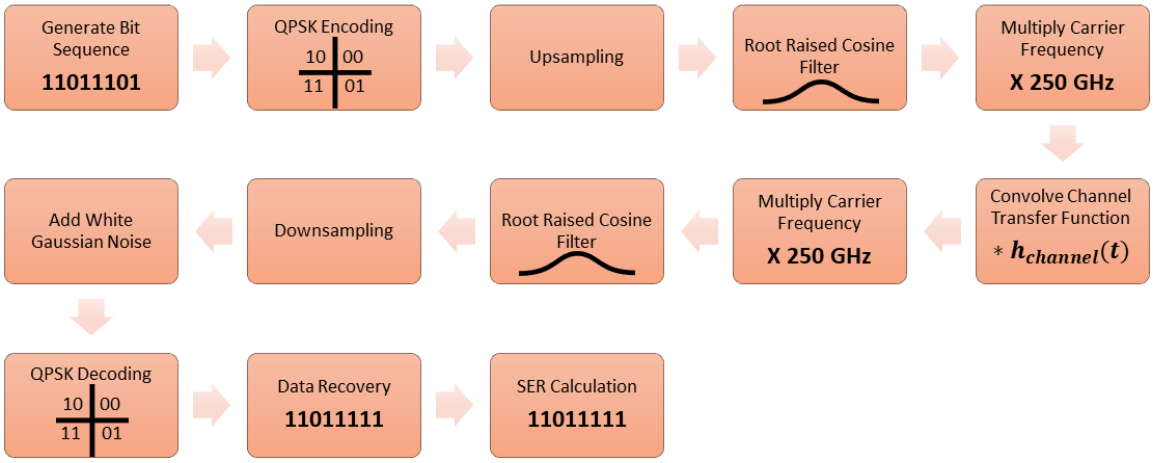

Fig. 19: Block diagram of the QPSK simulation used to measure the effects of GDD.

To quantify how scattering from rough surfaces affects the relationship between data rate and SER, a communication system was simulated in MATLAB® at 0.25 THz [39], [40]. A simple block diagram of the simulation is shown in Fig. 19. The simulation generates a pseudo-random symbol stream, splits the data into I and Q channels, and then modulates the two channels onto the carrier at 0.25 THz, using phase shift keying. This results in a quadrature phase shift keying

(QPSK) modulation scheme, which offers 2 data bits per symbol. The propagated communication signal takes the form of the following equation (8).

$$s(t) = \frac{A}{\sqrt{2}} I(t) \cos 2\pi f_c t - \frac{A}{\sqrt{2}} Q(t) \sin 2\pi f_c t \quad (8)$$

Next the time domain QPSK signal is converted into the frequency domain by a Fourier transform and multiplied by the channel transfer function. This channel transfer function was generated by the rough surface model described earlier in this chapter. After the signal has been multiplied by the channel transfer function, it is converted back into the time domain using the inverse Fourier transform. This accounts for all the effects caused by the rough surface. White Gaussian noise is then added to the channel to model a real system more accurately. After the noise is added, the signal is then demodulated.

At this point the received data is compared to the transmitted data to calculate the SER. Symbol rates of 10, 30 and 50 GBd were chosen to test the channel. Additive white Gaussian noise was added to the signal to achieve an SNR of 50 dB (as measured at the receiver after filtering), implying the SNR is not a limiting factor. The simulation was run iteratively over a wide range of surface height standard deviations, and for every value of standard deviation, a new random reflection surface was generated by our scattering model. For each surface, the simulation then sends approximately 1.1 million pseudo-random symbols through the channel and calculates the SER. This entire process was repeated 200 times, each time with a new randomized surface. Finally, all the calculated SER results were averaged to produce the presented SER results (next section). The averaging is very important to calculate the SER of the system. Due to the stochastic nature of the GDD produced by the rough surface, it is possible to produce very high and low SERs with the same surface height distribution parameters. Some surfaces generated produce zero errors, while others can cause a SER of 1. By averaging multiple runs together, an estimated SER can be found.

Section 5: Simulation Results – Single Reflection

Fig. 20 shows the averaged SERs and demonstrates how errors increase as the standard deviation of scatterer size (surface roughness) increases. It is of particular importance that symbol errors are almost non-existent up to a certain surface roughness (deemed the "dispersion limit"), at which point they abruptly turn on and then quickly reach levels that would render the communication system almost unusable. This threshold appears to occur when $\sigma \sim 0.28\lambda$–0.35λ, which is sensible considering this means the roughness is a significant fraction of the wavelength. As expected, higher symbol rates result in worse SER, since bits would be spaced more closely together in time, giving greater opportunity for ISI. While this does not appear to change the dispersion limit significantly, it does result in orders of magnitude higher SER once dispersion-induced symbol errors begin to occur. The large SNR of 50 dB means these effects are almost entirely due to dispersion alone. Lower SNRs would be expected to produce larger SERs. Upon preliminary investigation, the jagged appearance of the simulation data is due to the random nature of the rough surfaces. As stated earlier, the random occurrences of large GDD spikes coinciding with the simulated channel bandwidth can produce numerous errors, while other surfaces produce no errors. This makes it very time-consuming to smooth outlier data with averaging. As is apparent in Fig. 18, the lower data rate links (e.g., 10 GBd) are more severely affected by this phenomenon because their operational bandwidth is narrower, which means the entire bandwidth of the link may be strongly affected by GDD.

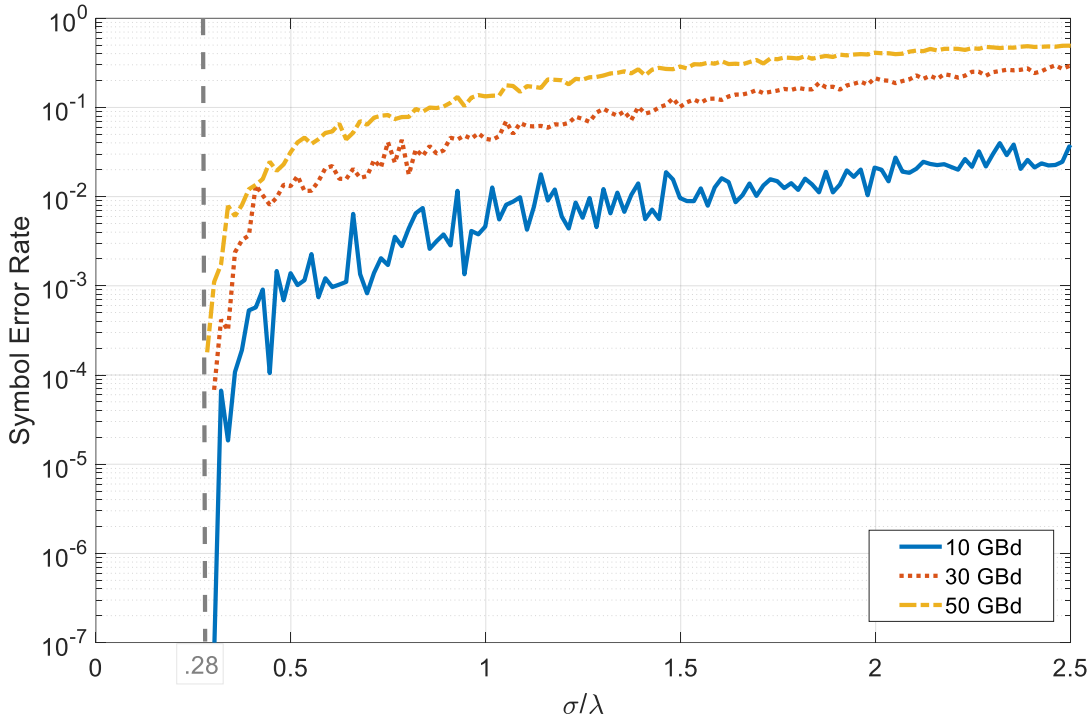

Fig. 20: Symbol error rates produced by a single reflection from a random diffuse surface whose height distribution standard deviation σ is expressed in fractions of a wavelength λ on the abscissa. Data is QPSK modulated at a 0.25 THz carrier frequency with a received SNR of 50 dB. Results shown are an average of 200 simulations from different random surface instances. [31]© 2021 IEEE

Section 6: Simulation Results – Multiple Reflections

Fig. 20 showed the effect caused by the dispersion resulting from a single reflection from a diffuse surface. Such effects, however, will accumulate when multiple reflections occur, which is important in the design of NLOS links. Fig. 21 shows the effect of multiple reflections on a 50 GBd data stream. This simulation was performed in the same manner as the previous simulation. For each reflection, a new random surface was generated. The effect of all the reflections is finally determined by the product of all the associated channel transfer functions. Multiple reflections are observed to shift the dispersion limit to smaller σ, meaning the channel is becoming more sensitive to the texture of the surfaces. At 5 reflections, which is here assumed to

be the maximum encountered in practical NLOS systems, the dispersion limit has reduced to σ ~ 0.18λ–0.20λ. Moreover, the SER beyond that limit is truly abysmal, quickly reaching 0.50 and trending to 0.75 as σ grows to multiple wavelengths. An SER = 0.75 corresponds to a complete loss of the original data stream [31].

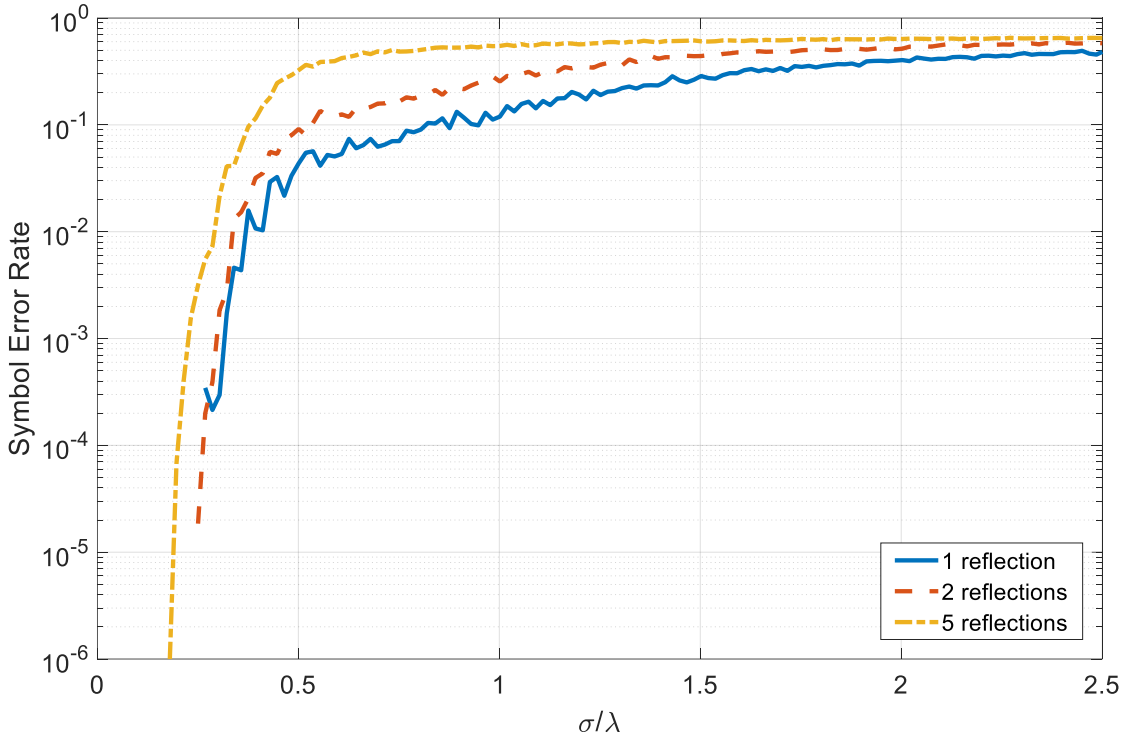

Fig. 21: Symbol error rates produced by multiple reflections from random diffuse surfaces whose height distribution standard deviation σ is expressed in fractions of a wavelength λ on the abscissa. Data is QPSK modulated at a 0.25 THz carrier frequency with a received SNR of 50 dB. Results shown are an average of 200 simulations from multiple random surface incidences. [31]© 2021 IEEE

CHAPTER V

CONCLUSION

Due to the unique properties of terahertz radiation, it is important for terahertz communication models to be as accurate as possible. Economical and easy to implement methods for manipulating terahertz radiation have been made using mixtures of aluminum powder and indoor paints in this thesis. These advancements will assist in the implementation of terahertz radiation for communications purposes.

Aluminum powder can be added to paint to increase the reflectivity of the surface. For an indoor environment, this improves the ability to contain the signal to improve the in a room. This can also be used to prevent a signal from entering areas where the signal is unused. In addition, reflective textured surfaces can be effectively used to spread THz beams by the process of scattering. As shown in this work, coarse Al powder was mixed with paint to create a rough textured surface. These two factors can be combined to improve THz NLOS communications. The increase in reflectivity can increase the signal strength at the receiver of a communications link, while a scattering surface can be used to increase the probability of a signal reaching a receiver.

An accurate model was needed to be made to recreate features found in the scattered terahertz signals. This allowed for large scale testing of how rough surfaces affect terahertz

radiation. Using a summation of multiple copies of a signal from a flat surface with random time delays, it is possible to recreate the reflected signal from a rough surface. This method, similar to Dikmelik, gives a very accurate representation of the scattered signal in both the time and frequency domains.

Using the modeled and measured data, the GDD caused by rough surfaces was measured and found to be significant. Applying these effects to a simulated QPSK communications system, an important, novel result was found. This result of these simulations is a dispersion limit at a surface roughness around $\sigma \sim 0.28\lambda–0.35\lambda$. At this point, the roughness of the surface becomes capable of causing bit errors in the transmitted signal. This result indicates a limitation to any THz NLOS link relying on scattered radiation. Due to this limit being primarily caused by ISI, no increase in power at the transmitter of link will improve the received data. Exacerbating this problem, the effect of dispersion increases with multiple reflections and higher baud rates.

In conclusion, this thesis shows that terahertz radiation can be manipulated by economical wall covering made by mixing aluminum powder and paint. This work shows the effects of GDD caused by rough surface reflections con communication channels and the limit at which the surface roughness begins to negatively affect SER. Further work can be done on improving the scattering model. Physical terahertz communication systems should be used in the future to further investigate the effects of GDD on large bandwidth links and confirm the findings of the simulations.

REFERENCES

[1] T. Kleine-Ostmann and T. Nagatsuma, "A Review on Terahertz Communications Research," *J. Infrared Millim. Terahertz Waves*, vol. 32, no. 2, pp. 143–171, Feb. 2011, doi: 10.1007/s10762-010-9758-1.

[2] H.-J. Song and T. Nagatsuma, "Present and Future of Terahertz Communications," *IEEE Trans. Terahertz Sci. Technol.*, vol. 1, no. 1, pp. 256–263, Sep. 2011, doi: 10.1109/TTHZ.2011.2159552.

[3] M. Drago, T. Azzino, M. Polese, Č. Stefanović, and M. Zorzi, "Reliable Video Streaming over mmWave with Multi Connectivity and Network Coding," in *2018 International Conference on Computing, Networking and Communications (ICNC)*, Mar. 2018, pp. 508–512. doi: 10.1109/ICCNC.2018.8390387.

[4] S. Saravanan and P. Sudhakar, "Telemedicine communication system in Mobile units," in *2017 International Conference on Computer Communication and Informatics (ICCCI)*, Jan. 2017, pp. 1–4. doi: 10.1109/ICCCI.2017.8117750.

[5] R. De', N. Pandey, and A. Pal, "Impact of digital surge during Covid-19 pandemic: A viewpoint on research and practice," *Int. J. Inf. Manag.*, vol. 55, p. 102171, Dec. 2020, doi: 10.1016/j.ijinfomgt.2020.102171.

[6] N. Khalid, N. A. Abbasi, and O. B. Akan, "300 GHz Broadband Transceiver Design for Low-THz Band Wireless Communications in Indoor Internet of Things," in *2017 IEEE International Conference on Internet of Things (iThings) and IEEE Green Computing and Communications (GreenCom) and IEEE Cyber, Physical and Social Computing (CPSCom) and IEEE Smart Data (SmartData)*, Jun. 2017, pp. 770–775. doi: 10.1109/iThings-GreenCom-CPSCom-SmartData.2017.118.

[7] J. Ma, R. Shrestha, L. Moeller, and D. M. Mittleman, "Invited Article: Channel performance for indoor and outdoor terahertz wireless links," *APL Photonics*, vol. 3, no. 5, p. 051601, May 2018, doi: 10.1063/1.5014037.

[8] "Radio Spectrum Allocation," *Federal Communications Commission*, Mar. 02, 2011. https://www.fcc.gov/engineering-technology/policy-and-rules-division/general/radio-spectrum-allocation (accessed Nov. 12, 2021).

[9] S. Priebe, C. Jastrow, M. Jacob, T. Kleine-Ostmann, T. Schrader, and T. Kürner, "Channel and Propagation Measurements at 300 GHz," *IEEE Trans. Antennas Propag.*, vol. 59, no. 5, pp. 1688–1698, May 2011, doi: 10.1109/TAP.2011.2122294.

[10] F. Sheikh, D. Lessy, M. Alissa, and T. Kaiser, "A Comparison Study of Non-specular Diffuse Scattering Models at Terahertz Frequencies," in *2018 First International Workshop on Mobile Terahertz Systems (IWMTS)*, Jul. 2018, pp. 1–6. doi: 10.1109/IWMTS.2018.8454692.

[11] J. Federici and L. Moeller, “Review of terahertz and subterahertz wireless communications,” *J. Appl. Phys.*, vol. 107, no. 11, p. 111101, Jun. 2010, doi: 10.1063/1.3386413.
[12] J. Ma, R. Shrestha, W. Zhang, L. Moeller, and D. M. Mittleman, “Terahertz Wireless Links Using Diffuse Scattering From Rough Surfaces,” *IEEE Trans. Terahertz Sci. Technol.*, vol. 9, no. 5, pp. 463–470, Sep. 2019, doi: 10.1109/TTHZ.2019.2933166.
[13] R. Piesiewicz, C. Jansen, D. Mittleman, T. Kleine-Ostmann, M. Koch, and T. Kurner, “Scattering Analysis for the Modeling of THz Communication Systems,” *IEEE Trans. Antennas Propag.*, vol. 55, no. 11, pp. 3002–3009, Nov. 2007, doi: 10.1109/TAP.2007.908559.
[14] C. Jansen *et al.*, “Diffuse Scattering From Rough Surfaces in THz Communication Channels,” *IEEE Trans. Terahertz Sci. Technol.*, vol. 1, no. 2, pp. 462–472, Nov. 2011, doi: 10.1109/TTHZ.2011.2153610.
[15] J. A. Colla, R. E. M. Vickers, M. Nancarrow, and R. A. Lewis, “3D Printing Metallised Plastics as Terahertz Reflectors,” *J. Infrared Millim. Terahertz Waves*, vol. 40, no. 7, pp. 752–762, Jul. 2019, doi: 10.1007/s10762-019-00596-y.
[16] Y. Zhang *et al.*, “Broadband diffuse terahertz wave scattering by flexible metasurface with randomized phase distribution,” *Sci. Rep.*, vol. 6, no. 1, p. 26875, May 2016, doi: 10.1038/srep26875.
[17] R. Piesiewicz, T. Kleine-Ostmann, N. Krumbholz, D. Mittleman, M. Koch, and T. Kürner, “Terahertz characterisation of building materials,” *Electron. Lett.*, vol. 41, no. 18, pp. 1002–1004, Sep. 2005, doi: 10.1049/el:20052444.
[18] L. Liang *et al.*, “Anomalous Terahertz Reflection and Scattering by Flexible and Conformal Coding Metamaterials,” *Adv. Opt. Mater.*, vol. 3, no. 10, pp. 1374–1380, 2015, doi: 10.1002/adom.201500206.
[19] M. Moccia *et al.*, “Suboptimal Coding Metasurfaces for Terahertz Diffuse Scattering,” *Sci. Rep.*, vol. 8, no. 1, p. 11908, Aug. 2018, doi: 10.1038/s41598-018-30375-z.
[20] J. Y. Dai *et al.*, “Wireless Communications through a Simplified Architecture Based on Time-Domain Digital Coding Metasurface,” *Adv. Mater. Technol.*, vol. 4, no. 7, p. 1900044, 2019, doi: 10.1002/admt.201900044.
[21] Y. Qi, B. Zhang, J. Ding, T. Zhang, X. Wang, and Z. Yi, “Efficient Manipulation of Terahertz waves by multi-bit Coding Metasurfaces and its further application,” *Chin. Phys. B*, vol. 30, no. 2, p. 024211, Dec. 2020, doi: 10.1088/1674-1056/abd6fc.
[22] B. Sima, K. Chen, X. Luo, J. Zhao, and Y. Feng, “Combining Frequency-Selective Scattering and Specular Reflection Through Phase-Dispersion Tailoring of a Metasurface,” *Phys. Rev. Appl.*, vol. 10, no. 6, p. 064043, Dec. 2018, doi: 10.1103/PhysRevApplied.10.064043.
[23] A. Momeni, K. Rouhi, H. Rajabalipanah, and A. Abdolali, “An Information Theory-Inspired Strategy for Design of Re-programmable Encrypted Graphene-based Coding Metasurfaces at Terahertz Frequencies,” *Sci. Rep.*, vol. 8, no. 1, p. 6200, Apr. 2018, doi: 10.1038/s41598-018-24553-2.
[24] Y. K. Srivastava, L. Cong, and R. Singh, “Dual-surface flexible THz Fano metasensor,” *Appl. Phys. Lett.*, vol. 111, no. 20, p. 201101, Nov. 2017, doi: 10.1063/1.5000428.
[25] X. Li, L. Lin, L. Wu, W. Yin, and J. Mao, “A Bandpass Graphene Frequency Selective Surface With Tunable Polarization Rotation for THz Applications,” *IEEE Trans. Antennas Propag.*, vol. 65, no. 2, pp. 662–672, Feb. 2017, doi: 10.1109/TAP.2016.2633163.
[26] Y. Guo, T. Zhang, W.-Y. Yin, and X.-H. Wang, “Improved Hybrid FDTD Method for Studying Tunable Graphene Frequency-Selective Surfaces (GFSS) for THz-Wave Applications,” *IEEE Trans. Terahertz Sci. Technol.*, vol. 5, no. 3, pp. 358–367, May 2015, doi: 10.1109/TTHZ.2015.2399105.

[27] X. Li *et al.*, “Investigation of Frequency-Selective Surfaces for a THz Gyromultiplier Output System,” *IEEE Trans. Electron Devices*, vol. 64, no. 11, pp. 4678–4685, Nov. 2017, doi: 10.1109/TED.2017.2746718.
[28] J. C. Wei, H. Chen, X. Qin, and T. J. Cui, “Surface and Volumetric Scattering by Rough Dielectric Boundary at Terahertz Frequencies,” *IEEE Trans. Antennas Propag.*, vol. 65, no. 6, pp. 3154–3161, Jun. 2017, doi: 10.1109/TAP.2017.2690307.
[29] D. A. DiGiovanni, A. J. Gatesman, R. H. Giles, T. M. Goyette, and W. E. Nixon, “Electromagnetic scattering from dielectric surfaces at millimeter wave and terahertz frequencies,” in *Passive and Active Millimeter-Wave Imaging XVIII*, May 2015, vol. 9462, p. 94620H. doi: 10.1117/12.2179707.
[30] Y. Dikmelik, J. B. Spicer, M. J. Fitch, and R. Osiander, “Effects of surface roughness on reflection spectra obtained by terahertz time-domain spectroscopy,” *Opt. Lett.*, vol. 31, no. 24, pp. 3653–3655, Dec. 2006, doi: 10.1364/OL.31.003653.
[31] R. Messenger, K. Strecker, S. Ekin, and J. F. O’Hara, “Dispersion From Diffuse Reflectors and Its Effect on Terahertz Wireless Communication Performance,” *IEEE Trans. Terahertz Sci. Technol.*, vol. 11, no. 6, pp. 695–703, Nov. 2021, doi: 10.1109/TTHZ.2021.3115725.
[32] G. S. Mudholkar and A. D. Hutson, “The epsilon–skew–normal distribution for analyzing near-normal data,” *J. Stat. Plan. Inference*, vol. 83, no. 2, pp. 291–309, Feb. 2000, doi: 10.1016/S0378-3758(99)00096-8.
[33] N. Duboust *et al.*, “An optical method for measuring surface roughness of machined carbon fibre-reinforced plastic composites,” *J. Compos. Mater.*, vol. 51, no. 3, pp. 289–302, Feb. 2017, doi: 10.1177/0021998316644849.
[34] D. Grischkowsky, S. Keiding, M. van Exter, and C. Fattinger, “Far-infrared time-domain spectroscopy with terahertz beams of dielectrics and semiconductors,” *JOSA B*, vol. 7, no. 10, pp. 2006–2015, Oct. 1990, doi: 10.1364/JOSAB.7.002006.
[35] B. Sklar, “Rayleigh fading channels in mobile digital communication systems .I. Characterization,” *IEEE Commun. Mag.*, vol. 35, no. 7, pp. 90–100, Jul. 1997, doi: 10.1109/35.601747.
[36] G. P. Agrawal, *Fiber-Optic Communication Systems*, 4th edition. New York: Wiley, 2010.
[37] M. Mandehgar, Y. Yang, and D. Grischkowsky, “Experimental confirmation and physical understanding of ultra-high bit rate impulse radio in the THz digital communication channels of the atmosphere,” *J. Opt.*, vol. 16, no. 9, p. 094004, Sep. 2014, doi: 10.1088/2040-8978/16/9/094004.
[38] K. Strecker, S. Ekin, and J. F. O’Hara, “Compensating Atmospheric Channel Dispersion for Terahertz Wireless Communication,” *Sci. Rep.*, vol. 10, no. 1, p. 5816, Apr. 2020, doi: 10.1038/s41598-020-62692-7.
[39] S. O. Popescu, A. S. Gontean, and D. Ianchis, “Implementation of a QPSK system on FPGA,” in *2011 IEEE 9th International Symposium on Intelligent Systems and Informatics*, Sep. 2011, pp. 365–370. doi: 10.1109/SISY.2011.6034354.
[40] A. Goldsmith, *Wireless Communications*. Cambridge: Cambridge University Press, 2005. doi: 10.1017/CBO9780511841224.

VITA

Russ Thomas Messenger

Candidate for the Degree of

Master of Science

Thesis: TERAHERTZ DIFFUSE REFLECTORS AND THEIR EFFECTS ON GROUP DELAY DISPERSION AND COMMUNICATION PERFORMANCE

Major Field: Electrical Engineering

Biographical:

Education:

Completed the requirements for the Master of Science in Electrical Engineering at Oklahoma State University, Stillwater, Oklahoma in December 2021.

Completed the requirements for the Bachelor of Science in Electrical Engineering at Oklahoma State University, Stillwater, Oklahoma in 2019.

Experience:

Graduate Research Assistant, Ultrafast Optoelectronics Laboratory, Oklahoma State University (2019-2021)

Graduate Teaching Assistant, Data Communications, Oklahoma State University (2019-2021)

Professional Memberships: SPIE Student Member

Publications:

R. Messenger, K. Strecker, S. Ekin and J. F. O'Hara, "Dispersion From Diffuse Reflectors and Its Effect on Terahertz Wireless Communication Performance," in IEEE Transactions on Terahertz Science and Technology, vol. 11, no. 6, pp. 695-703, Nov. 2021, doi: 10.1109/TTHZ.2021.3115725.